Distributed Subsurface Imaging with Tikhonov and Total Variation Regularization for Seismic Networks

Ban-Sok Shin and Dmitriy Shutin
German Aerospace Center - Institute of Communications and Navigation
{ban-sok.shin, dmitriy.shutin}@dlr.de

***Abstract*—Future space exploration missions envision multi-agent networks autonomously conducting subsurface exploration. Achieving this requires distributed subsurface imaging. Previously, we introduced the adapt-then-combine full waveform inversion (ATCFWI) in both the time and frequency domains, enabling each receiver in a seismic network to generate high-resolution subsurface images locally through data exchange with neighboring receivers. To further enhance imaging quality, we explore the regularization of local cost functions. Specifically, we incorporate Tikhonov and total variation (TV) regularization. Tikhonov regularization promotes smooth structural recovery, while TV regularization enhances edge sharpness and contrast. We integrate both methods into ATCFWI to enable robust imaging in a distributed fashion. Through numerical evaluations, we demonstrate that ATCFWI, combined with these regularization techniques, significantly improves imaging performance across all receivers. Code for our proposed method is available on https://github.com/bshin/fd-atcfwi.**

***Index Terms*—Full waveform inversion, seismic imaging, multi-agent seismic exploration, distributed imaging**

I. Introduction

Detecting lava tubes or caves on the Moon and Mars is a key challenge for future planetary exploration. These subsurface structures offer significant advantages, including stable temperatures and natural protection from cosmic radiation, making them promising candidates for astronaut habitats and equipment storage in upcoming space missions [1], [2], [3]. To gain a deeper understanding of the lunar and Martian subsurface and to identify such structures, autonomous multi-agent systems have been proposed [4], [5], [6].

One potential approach involves deploying robotic agents equipped with geophones to record seismic measurements, as illustrated in Fig. 1. These measurements are then used to collaboratively image relevant subsurface structures within the multi-agent network. Additionally, the measurement positions of the agents are optimized based on the current subsurface estimates to refine imaging results. Implementing such a system requires distributed data processing to effectively solve the imaging problem in a cooperative manner. This allows each agent to estimate the subsurface structure without direct access to all measurement data within the network. Each agent can then utilize this estimate to reposition itself for improved sampling and enhanced imaging accuracy. To achieve this, we previously proposed the frequency-domain adapt-then-combine full waveform inversion (FD-ATCFWI), a method that enables high-resolution subsurface imaging in a distributed fashion [7]. Specifically, each agent obtains a global subsurface image through data exchange with only its direct neighbors. The resulting estimate closely approximates the centralized imaging outcome of traditional full waveform inversion (FWI) while remaining independent of the agent's sampling position.

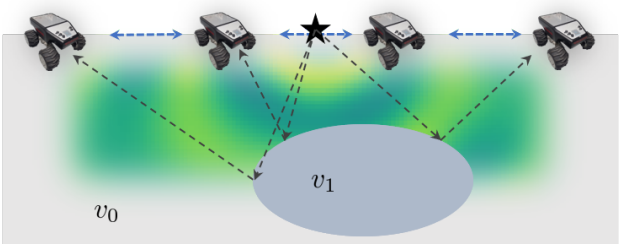

Fig. 1: Concept of a multi-agent network performing 2D subsurface imaging. A source $\star$ is placed on the surface and the agents measure seismic data using an on-board geophone. The goal is to obtain subsurface images in a cooperative fashion by data exchange over wireless connections (blue arrows) among the agents.

In this work, we investigate the regularization of the cost functional in FD-ATCFWI to further enhance imaging quality. Inspired by [8], we incorporate a combination of Tikhonov and total variation (TV) regularization to improve the accuracy of high-contrast structures and anomaly recovery. We demonstrate that, particularly in noisy environments, this regularization significantly enhances imaging quality across all receivers compared to using the standard cost functional. Furthermore, we show that FD-ATCFWI inherently provides robustness against measurement noise due to its built-in data exchange averaging mechanism.

II. Distributed Subsurface Imaging

We first introduce the seismic network model before giving a brief review of the (centralized) FWI in the frequency domain. Afterwards, we introduce our proposed FD-ATCFWI with Tikhonov and TV regularization.

A. Seismic network model

We assume an array of N_{R} seismic receivers or geophones arranged in a line on the surface above the domain of interest Ω. Each receiver r is associated with a set of neighbors $\mathcal{N}_r$, which includes all receivers ℓ capable of bidirectional data exchange with r as well as r itself. Moreover, we assume that the network forms a connected graph, ensuring that any two

receivers are reachable via a multi-hop connection, preventing any separation of the network graph.

B. Frequency-Domain Full Waveform Inversion

We briefly review full waveform inversion (FWI) in the frequency domain to provide context of our proposed method. In FWI we seek a subsurface model $\mathbf{m} \in \mathbb{R}^{N_\mathrm{x} N_\mathrm{z}}$ that represents spatial distribution of a material parameter such as wave velocity, density, etc. $N_\mathrm{x}, N_\mathrm{z}$ are the number of grid cells in the two-dimensional discretized subsurface domain Ω. This can be achieved by matching predicted, synthesized seismic data $\mathbf{d}_s^{\mathrm{syn}} \in \mathbb{C}^{N_\mathrm{R}}$ to observed data $\mathbf{d}_s^{\mathrm{obs}} \in \mathbb{C}^{N_\mathrm{R}}$ from N_R receivers by iteratively adapting the parameter $\mathbf{m}$. Note that the data is assumed to be in the frequency domain and is therefore in general complex. For N_S source positions and a specific frequency ω the optimization problem in FWI can be formulated as

$$\min_{\mathbf{m}} \mathcal{J}(\mathbf{m}) = \frac{1}{2} \sum_{s=1}^{N_\mathrm{S}} || \underbrace{\mathbf{P}^\mathsf{T} \mathbf{u}_s(\omega, \mathbf{m})}_{\mathbf{d}_s^{\mathrm{syn}}(\omega, \mathbf{m})} - \mathbf{d}_s^{\mathrm{obs}}(\omega) ||_2^2 + \mathcal{R}(\mathbf{m}) \tag{1a}$$

$$\text{s.t.} \quad \mathbf{A}(\omega, \mathbf{m}) \mathbf{u}_s(\omega, \mathbf{m}) = \mathbf{f}_s(\omega). \tag{1b}$$

The functional $\mathcal{R}(\mathbf{m})$ denotes a regularization term that integrates prior assumptions on $\mathbf{m}$ into the optimization problem. Furthermore, $\mathbf{P} \in \mathbb{R}^{N_\mathrm{x} N_\mathrm{z} \times N_\mathrm{R}}$ is a sampling matrix that extracts the predicted data at the respective receiver positions from the synthesized wavefield $\mathbf{u}_s(\omega, \mathbf{m}) \in \mathbb{C}^{N_\mathrm{x} N_\mathrm{z}}$. This wavefield is obtained by solving the Helmholtz equation that describes wave propagation in the frequency domain. Assuming finite-difference approximation, the Helmholtz equation can be expressed by the linear system of equations given in (1b). Here, $\mathbf{A}(\omega, \mathbf{m}) \in \mathbb{C}^{N_\mathrm{x} N_\mathrm{z} \times N_\mathrm{x} N_\mathrm{z}}$ is the discretized forward operator, $\mathbf{u}_s(\omega, \mathbf{m}) \in \mathbb{C}^{N_\mathrm{x} N_\mathrm{z}}$ the wavefield in the frequency domain and $\mathbf{f}_s(\omega) \in \mathbb{C}^{N_\mathrm{x} N_\mathrm{z}}$ the source signal also in frequency domain at frequency ω and for source s. Regarding $\mathbf{d}_s^{\mathrm{obs}}(\omega)$, we assume additive zero-mean white Gaussian noise $\mathbf{n} \in \mathbb{C}^{N_\mathrm{R}}$ on the wavefield amplitudes:

$$\mathbf{d}_s^{\mathrm{obs}} = \mathbf{P}^\mathsf{T} \mathbf{u}_s(\omega, \mathbf{m}^\star) + \mathbf{n} \tag{2}$$

where $\mathbf{m}^\star$ is the true (discretized) subsurface model. To find a suitable subsurface model $\mathbf{m}$ iteratively, the gradient of $\mathcal{J}(\mathbf{m})$ wrt. $\mathbf{m}$ is required. However, (1a) is constrained by the partial differential equation (PDE) in (1b) and thus, calculation of the derivative is not straightforward. For such optimization problems the *adjoint-state method* can be used which essentially employs Lagrange multipliers, cf. [9]. It avoids costly computations of the Jacobian matrix, i.e., the sensitivities of the observed data wrt. the model parameters $\mathbf{m}$, but requires numerical solution of two PDEs. With the FWI gradient available, numerical optimization schemes such as nonlinear conjugate gradient or quasi-Newton methods can be applied to iteratively approach a suitable subsurface model, cf. [10].

C. Frequency-Domain Adapt-Then-Combine Full Waveform Inversion

In the following, we introduce the frequency-domain adapt-then-combine full waveform inversion (FD-ATCFWI) which we proposed in [7]. In contrast to traditional FWI, FD-ATCFWI allows for distributed subsurface imaging within a network of seismic receivers. In particular, the receivers do not need to be connected in a full mesh topology. As long as the network topology builds a connected graph, the FD-ATCFWI enables receivers to achieve estimates of the complete subsurface locally by sharing data only with connected neighboring receivers.

Different from [7] where no regularization has been considered we introduce FD-ATCFWI here with the possibility of integrating regularization into the imaging framework. As a first step, we separate the global FWI cost (1a) for a single frequency ω over the N_R receivers in the network, i.e.,

$$\mathcal{J}(\mathbf{m}, \omega) = \sum_{r=1}^{N_\mathrm{R}} \mathcal{J}_r(\mathbf{m}, \omega) \tag{3}$$

with

$$\mathcal{J}_r(\mathbf{m}, \omega) = \frac{1}{2} \sum_s |\mathbf{p}_r^\mathsf{T} \mathbf{u}_s(\omega, \mathbf{m}) - d_{s,r}^{\mathrm{obs}}(\omega)|^2 + \mathcal{R}_r(\mathbf{m}). \tag{4}$$

Here, $\mathcal{R}_r(\mathbf{m})$ denotes a receiver-specific regularization term on the subsurface estimate $\mathbf{m}$ and $\mathbf{p}_r$ is the r-th column of sampling matrix $\mathbf{P}$. To reconstruct a subsurface image locally at each receiver r we apply the adapt-then-combine technique [11]. To this end, we introduce receiver-specific subsurface models $\mathbf{m}_r$ and calculate the gradient of $\mathcal{J}_r(\mathbf{m}_r, \omega)$ wrt. $\mathbf{m}_r$ using the adjoint-state method:

$$\frac{\mathrm{d}\mathcal{J}_r(\mathbf{m}_r)}{\mathrm{d}\mathbf{m}_r} = \mathrm{Re}\left\{ \sum_s \omega^2 \boldsymbol{\lambda}_{s,r}^*(\omega, \mathbf{m}_r) \odot \mathbf{u}_{s,r}(\omega, \mathbf{m}_r) \right\} + \frac{\mathrm{d}\mathcal{R}_r(\mathbf{m}_r)}{\mathrm{d}\mathbf{m}_r} = \delta \mathbf{m}_r \tag{5}$$

Here, $*$ denotes complex conjugate of the matrix entries and $\odot$ is an element-wise multiplication. The gradient $\delta \mathbf{m}_r$ is now specific to receiver r based on its model $\mathbf{m}_r$. The variable $\boldsymbol{\lambda}_s(\omega, \mathbf{m}_r) \in \mathbb{C}^{N_\mathrm{x} N_\mathrm{z}}$ is the adjoint-state wavefield (or the Lagrange multiplier) which is computed by solving the following linear system of equations for each source s:

$$\mathbf{A}^\mathsf{H}(\omega, \mathbf{m}_r) \boldsymbol{\lambda}_{s,r}(\omega, \mathbf{m}_r) = \mathbf{p}_r^\mathsf{T} \mathbf{u}_{s,r}(\omega, \mathbf{m}_r) - d_{s,r}^{\mathrm{obs}}(\omega) \tag{6}$$

In (6) we need to solve an adapted Helmholtz equation where the data residuals $\mathbf{u}_{s,r}(\omega, \mathbf{m}_r) - \mathbf{d}_{s,r}^{\mathrm{obs}}(\omega)$ are placed as source terms at the receiver positions. Finally, we apply the ATC to obtain update equations for each receiver's subsurface $\mathbf{m}_r$:

$$\text{(Adapt)} \quad \widetilde{\mathbf{m}}_r^{[k+1]} = \mathbf{m}_r^{[k]} + \alpha^{[k]} \sum_{\ell \in \mathcal{N}_r} a_{\ell r} \delta \mathbf{m}_\ell^{[k]} \tag{7a}$$

$$\text{(Combine)} \quad \mathbf{m}_r^{[k+1]} = \sum_{\ell \in \mathcal{N}_r} b_{\ell r} \widetilde{\mathbf{m}}_\ell^{[k+1]} \tag{7b}$$

Coefficients $a_{\ell r}, b_{\ell r} \geq 0$ are combination weights that determine how to weight gradients and subsurface models in the

data fusion process, cf. [11]. One simple choice that guarantees convergence is $a_{\ell r} = b_{\ell r} = 1/|\mathcal{N}_r|, \forall \ell \in \mathcal{N}_r$, which we also use in our evaluations.

III. Regularization for Subsurface Imaging

In the following, we introduce regularization terms which we integrate into FD-ATCFWI to enhance its imaging performance. When introducing the regularization functions and their respective derivatives we formulate these in the continuous domain to simplify understanding of the content. Thus, for the following description the subsurface is considered to be a continuous scalar function $m(\mathbf{x})$ over spatial coordinate $\mathbf{x}$.

A. Tikhonov Regularization

One of the most commonly used regularization terms is the Tikhonov regularization. In FWI it can be used in combination with a prior subsurface model $m_{\text{prior}}(\mathbf{x})$, cf. [10]:

$$\mathcal{R}^{\text{Tikh,1}}(m) = \frac{1}{2}\int_\Omega |m(\mathbf{x}) - m_{\text{prior}}(\mathbf{x})|^2 \,\mathrm{d}\mathbf{x}. \tag{8}$$

To calculate the respective derivative we make use of functional derivatives [12, Appendix D] resulting in

$$\frac{\mathrm{d}}{\mathrm{d}m}\mathcal{R}^{\text{Tikh,1}}(m) = m(\mathbf{x}) - m_{\text{prior}}(\mathbf{x}). \tag{9}$$

The function $\mathcal{R}_r^{\text{Tikh,1}}(m)$ penalizes significant changes from the prior subsurface model and therefore helps in reducing noise artifacts in the subsurface image.

Another possibility is to constrain the gradient of the subsurface model [8], i.e.,

$$\mathcal{R}^{\text{Tikh,2}}(m) = \int_\Omega |\nabla m(\mathbf{x})|^2 \,\mathrm{d}\mathbf{x}. \tag{10}$$

Similar to $\mathcal{R}^{\text{Tikh,1}}(m)$ it suppresses high-frequency noise artifacts and stabilizes the inversion process. In addition, it is useful for obtaining a smooth, low-frequency subsurface model that can be refined at higher frequencies. Its corresponding derivative wrt. m can be calculated via the Laplacian:

$$\frac{\mathrm{d}}{\mathrm{d}m}\mathcal{R}^{\text{Tikh,2}}(m) = -\nabla^2 m(\mathbf{x}). \tag{11}$$

B. Total Variation Regularization

In contrast to Tikhonov regularization $\mathcal{R}_r^{\text{Tikh,2}}$ which uses the ℓ_2-norm, the total variation (TV) regularization employs an ℓ_1-norm on the gradient of the subsurface model $m(\mathbf{x})$ [13]:

$$\mathcal{R}^{\text{TV}}(m) = \int_\Omega |\nabla m(\mathbf{x})| \,\mathrm{d}\mathbf{x}, \tag{12}$$

where $|\nabla m(\mathbf{x})| = |\frac{\partial}{\partial x} m(\mathbf{x})| + |\frac{\partial}{\partial z} m(\mathbf{x})|$. By using the ℓ_1-norm on ∇m the TV regularization is suitable for recovery of blocky structures and higher contrasts in the subsurface image. Calculating the derivative of $\mathcal{R}_r^{\text{TV}}(m)$ wrt. m is not possible in closed-form due to the non-differentiable ℓ_1-norm. One common approach to circumvent this issue is to use a smooth approximation of the ℓ_1-norm. Other possibilities include using proximal operators [13], primal-dual hybrid gradient [14] or the alternating direction method of multipliers [15]. To keep investigations simple we rely on a smooth approximation, i.e.,

$$\mathcal{R}^{\text{TV}}(m) = \int_\Omega \sqrt{|\nabla m(\mathbf{x})|^2 + \epsilon} \,\mathrm{d}\mathbf{x}, \tag{13}$$

where $\epsilon > 0$ determines how smoothly the ℓ_1-norm is approximated. While a high ϵ results in a smooth approximation, a low ϵ allows for improved approximation of the ℓ_1-norm and therefore, sharper edges in the image. However, choosing ϵ too small can lead to numerical instabilities and artifacts in the image. One heuristic rule is to select $\epsilon = c \cdot \max(|\nabla m(\mathbf{x}))|)$ where c is a small scaling factor in the range 10^{-4} to 10^{-2}. Finally, the derivative wrt. m can be calculated in closed-form:

$$\frac{\mathrm{d}}{\mathrm{d}m}\mathcal{R}^{\text{TV}}(m) = -\nabla \cdot \frac{\nabla m(\mathbf{x})}{\sqrt{|\nabla m(\mathbf{x})|^2 + \epsilon}}. \tag{14}$$

C. Combination of Tikhonov and TV Regularization

The regularization terms described previously can be combined to improve the imaging performance. To this end, we define for each receiver r:

$$\begin{aligned}\mathcal{R}_r(m) = \lambda_{\text{Tikh},1}\mathcal{R}_r^{\text{Tikh},1}(m) + \lambda_{\text{Tikh},2}\mathcal{R}_r^{\text{Tikh},2}(m) \\ + \lambda_{\text{TV}}\mathcal{R}_r^{\text{TV}}(m).\end{aligned} \tag{15}$$

The derivative of $\mathcal{R}_r(m)$ wrt. m is then given accordingly by the sum of the respective derivatives. This combined Tikhonov-Total variation (TT) regularization is used in (5) to adjust the receiver-specific gradient $\delta\mathbf{m}_r$ in FD-ATCFWI. From (7a) we see that in each iteration of FD-ATCFWI gradients from neighboring receivers are fused. Therefore, also data on the regularization terms from neighboring receivers are included into the receiver's local adaptation procedure of $\mathbf{m}_r$. The parameters $\lambda_{\text{Tikh},1}, \lambda_{\text{Tikh},2}, \lambda_{\text{TV}} > 0$ determine how to weight the different regularization terms. Balancing these parameters is crucial for good imaging performance especially for noisy measurements. Moreover, they usually depend on the SNR and need to be adjusted accordingly.

IV. Numerical Results

We investigate imaging performance of FD-ATCFWI with TT regularization for a synthetic subsurface model with an increasing velocity in the background and two elliptic anomalies with velocities $v_1 = 1.8\,\mathrm{km\,s^{-1}}$ and $v_2 = 1.6\,\mathrm{km\,s^{-1}}$. The spatial domain of size $1.4\,\mathrm{km} \times 0.5\,\mathrm{km}$ is discretized with a grid spacing of $\Delta x = \Delta z = 10\,\mathrm{m}$. We assume $N_\mathrm{R} = 24$ receivers and $N_\mathrm{S} = 20$ sources which are uniformly arranged over the surface. Furthermore, each receiver is connected to a maximum of three receivers to their left- and right-hand-side, respectively. The source signal is a Ricker wavelet with dominant frequency $f_{\text{dom}} = 6\,\mathrm{Hz}$. As starting model we use the background velocity model, i.e., we assume knowledge of the background model but no prior information about the elliptic anomalies. With regard to the frequencies we select the range $2\,\mathrm{Hz}$ to $8\,\mathrm{Hz}$ with a frequency step of $\Delta f = 1\,\mathrm{Hz}$. For both FD-ATCFWI and FWI we perform $N_{\text{FWI}} = 50$ iterations per frequency. After inversion of one frequency we employ the obtained $\mathbf{m}_r$ to initialize the subsurface model for the next

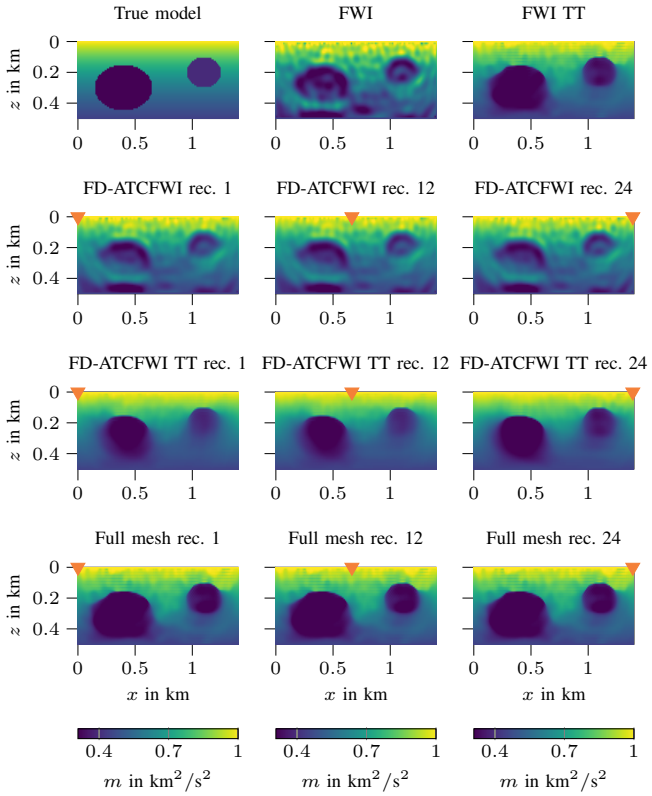

Fig. 2: Imaging results of FWI and FD-ATCFWI with TT regularization at $\mathrm{SNR} = 20\,\mathrm{dB}$. For FD-ATCFWI the respective receiver locations are indicated by ▼. The last row depicts results of FD-ATCFWI with TT and full mesh connectivity.

TABLE I: Selection of regularization parameters for FWI and FD-ATCFWI.

Method	$\lambda_{\mathrm{Tikh},1}$	$\lambda_{\mathrm{Tikh},2}$	λ_{TV}
FWI	10^{-9}	$3 \cdot 10^{-9}$	10^{-9}
FD-ATCFWI	$3 \cdot 10^{-10}$	$4 \cdot 10^{-10}$	$3.5 \cdot 10^{-10}$

frequency. As an initial step size we choose $\alpha^{[0]} = 0.01$ which is then exponentially reduced over the iterations to facilitate convergence. The selected regularization parameters for both FWI and FD-ATCFWI are summarized in Table I.

A. Imaging Results

Fig. 2 depicts the true squared slowness model and the recovered subsurface images by FWI and FD-ATCFWI with and without TT regularization for an $\mathrm{SNR} = 20\,\mathrm{dB}$. The noise variance corresponding to the SNR is computed based on the energy of the seismic traces averaged over all receivers. We observe that FWI is capable of recovering both anomalies but with strong artifacts due to measurement noise. Adding regularization enhances the imaging result significantly as can be seen for FWI TT. In a similar way, without regularization FD-ATCFWI obtains subsurface images with strong artifacts that severely reduce accuracy. Furthermore, while the outer shapes are reconstructed well amplitudes in the inner parts of the anomalies are not recovered with high accuracy. In contrast, when using TT regularization FD-ATCFWI is able to recover accurate subsurface images similar to FWI TT. In particular, the imaging results are coherent over all receivers independent of their sampling position and have significant reduction of noise artifacts. When using a full mesh connectivity the imaging results can be further enhanced resulting in nearly identical imaging results as for the centralized FWI TT.

B. Local Gradients and Subsurface Models

In Fig. 3 we show examples of receiver-specific gradients after the adapt step (7a) with neighboring gradient information for different frequencies using FD-ATCFWI with TT. Due to different receiver positions the respective gradients differ from each other. At 3 Hz, structures of the elliptic anomalies are only visible for the middle receiver. However, as the frequency increases and as such the information diffusion through the seismic network, contours of the anomalies become more visible. Here, one can also observe the effect of the TV regularization that enables sharp lines of the elliptic anomalies, see the example at 7 Hz.

Corresponding to Fig. 3, in Fig. 4 we show local subsurface models at different frequencies after the combine step (7b). We observe that at low frequencies rough structures of the anomalies are recovered while at higher frequencies details of the contour and the inner structure of the anomalies are revealed. Furthermore, especially at frequencies 3 Hz and 5 Hz anomalies are differently well recovered depending on the receiver location: The leftmost receiver can recover the left ellipse better than the right ellipse and vice versa for the rightmost receiver. As the frequency increases and therefore, also the number of data exchanges among the receivers this difference in reconstruction is reduced, cf. example at 7 Hz.

C. Error Curves

Fig. 5 depicts imaging performance in terms of normalized mean square error (NMSE) and structural similarity index measure (SSIM). The NMSE is computed between true model $\mathbf{m}^\star$ and estimated subsurface model $\mathbf{m}_r$ and then averaged over all receivers. The SSIM is a perception-based metric that is used to compare similarity between two images [16]. Since it includes structural information of the images it aligns better with human perspective of similarity. From Fig. 5 we observe that FD-ATCFWI with TT performs close to FWI with TT for both NMSE and SSIM. In terms of SSIM, one notices that FD-ATCFWI experiences less fluctuations for both TT and without regularization. This behavior is due to the averaging process among the receivers. Moreover, FD-ATCFWI without TT performs better than the corresponding FWI wrt. SSIM but worse in terms of NMSE. This shows that the SSIM reflects more accurately our perception of imaging quality in this case. For FD-ATCFWI with full mesh connectivity (fm.) we observe that it performs even closer to FWI TT confirming the imaging results depicted in Fig. 2.

V. Conclusion

We explored the integration of Tikhonov and total variation (TT) regularization for distributed subsurface imaging using

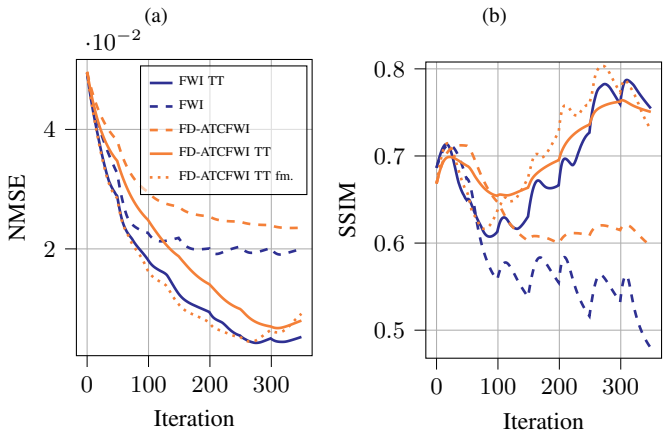

Fig. 5: (a) NMSE and (b) SSIM performance of FD-ATCFWI and FWI with and without TT for SNR $= 20\,\mathrm{dB}$. For FD-ATCFWI additionally full mesh (fm.) performance is shown.

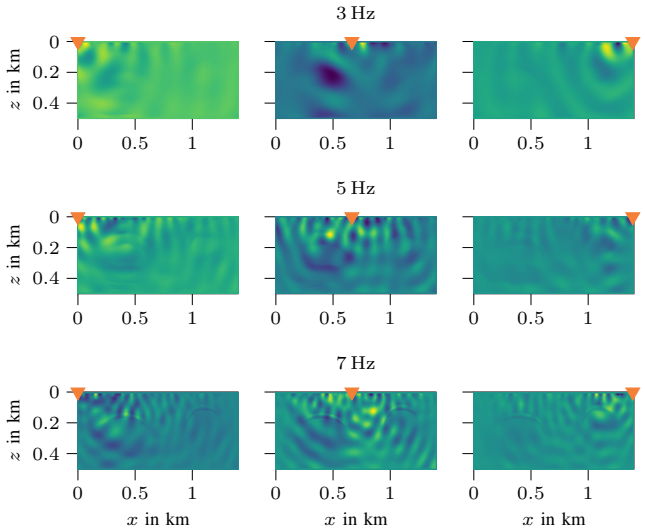

Fig. 3: Receiver-specific gradients after adapt step (7a) at $3\,\mathrm{Hz}, 5\,\mathrm{Hz}, 7\,\mathrm{Hz}$ for FD-ATCFWI with TT.

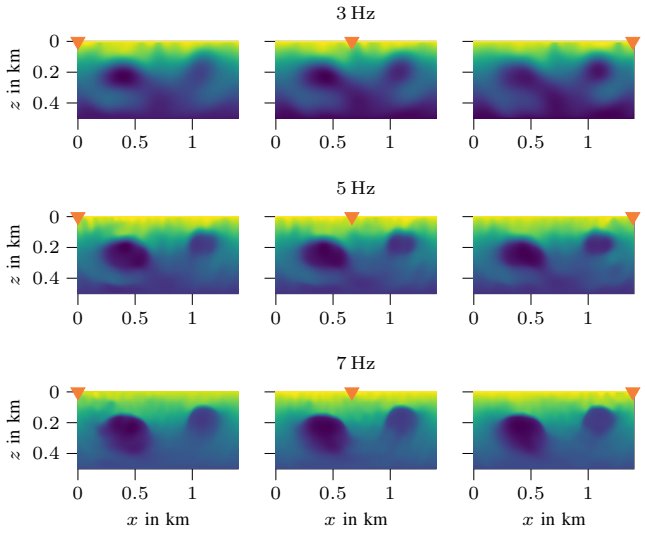

Fig. 4: Receiver-specific subsurface models after combine step (7b) at $3\,\mathrm{Hz}, 5\,\mathrm{Hz}, 7\,\mathrm{Hz}$ for FD-ATCFWI with TT.

adapt-then-combine full waveform inversion (FD-ATCFWI) in the frequency domain. Incorporating TT regularization into the distributed imaging framework significantly enhances imaging performance. In addition to reducing noise artifacts, this approach yields sharper anomaly contours, improving overall image clarity. We demonstrated that FD-ATCFWI with TT regularization achieves imaging quality comparable to centralized full waveform inversion (FWI) while remaining independent of receiver locations. These findings highlight FD-ATCFWI as a promising method for cooperative subsurface exploration in multi-agent networks.

VI. Acknowledgement

The work leading to this publication was partially funded by the German Research Foundation (DFG) under grants SH 1975/1-1 and SH 1743/3-1.

References

[1] H. Kalita, A. Quintero, A. Wissing *et al.*, "Evaluation of lunar pits and lava tubes for use as human habitats," in *Earth and Space 2021*. American Society of Civil Engineers, Apr. 2021, p. 944–957.

[2] S. Keil, H. Igel, M. Schimmel, F. Lindner, and F. Bernauer, "Investigating subsurface properties of the shallow lunar crust using seismic interferometry on synthetic and recorded data," *Earth and Space Science*, vol. 11, no. 10, Oct. 2024.

[3] M. Zhou, Z. Ye, R. Huang *et al.*, "High-resolution morphology of lunar lava tube pits using photogrammetric modeling of multiple stereo images," *Earth and Space Science*, vol. 11, no. 11, Nov. 2024.

[4] S. Keil, H. Igel, F. Bernauer *et al.*, "The NEPOS Project: Near-Surface Seismic Exploration of Planetary Bodies with Adaptive Networks," in *AGU Fall Meeting Abstracts*, vol. 2023, Dec. 2023, pp. P11C–2746.

[5] J.-P. de la Croix, F. Rossi, R. Brockers *et al.*, "Multi-agent autonomy for space exploration on the cadre lunar technology demonstration," in *2024 IEEE Aerospace Conference*. IEEE, Mar. 2024, p. 1–14.

[6] G. Rabideau, J. Russino, A. Branch *et al.*, "Planning, scheduling, and execution on the moon: the cadre technology demonstration mission," 2025. [Online]. Available: https://arxiv.org/abs/2502.14803

[7] B.-S. Shin and D. Shutin, "Distributed full waveform inversion in the frequency domain for seismic networks," *submitted for publication to IEEE Geoscience and Remote Sensing Letters*, 2025.

[8] H. S. Aghamiry, A. Gholami, and S. Operto, "Hybrid tikhonov + total-variation regularization for imaging large-contrast media by full-waveform inversion," in *SEG Technical Program*, 2018.

[9] R. E. Plessix, "A review of the adjoint-state method for computing the gradient of a functional with geophysical applications," *Geophys. J. Int.*, 2006.

[10] J. Virieux and S. Operto, "An overview of full-waveform inversion in exploration geophysics," *Geophysics*, vol. 74, no. 6, 2009.

[11] A. H. Sayed *et al.*, "Diffusion strategies for adaptation and learning over networks," *IEEE Signal Processing Magazine*, pp. 155–171, 2013.

[12] C. M. Bishop, *Pattern Recognition and Machine Learning (Information Science and Statistics)*. Berlin, Heidelberg: Springer-Verlag, 2006.

[13] A. Kadu, H. Mansour, and P. T. Boufounos, "High-contrast reflection tomography with total-variation constraints," *IEEE Trans. Comput. Imaging*, vol. 6, pp. 1523–1536, 2020.

[14] E. Esser, L. Guasch, T. van Leeuwen, A. Y. Aravkin, and F. J. Herrmann, "Total variation regularization strategies in full-waveform inversion," *SIAM Journal on Imaging Sciences*, vol. 11, pp. 376–406, 2018.

[15] H. S. Aghamiry, A. Gholami, and S. Operto, "Full waveform inversion by proximal newton method using adaptive regularization," *Geophysical Journal International*, vol. 224, pp. 169–180, 2021.

[16] Z. Wang, A. Bovik, H. Sheikh, and E. Simoncelli, "Image quality assessment: from error visibility to structural similarity," *IEEE Trans. Image Process.*, vol. 13, no. 4, p. 600–612, Apr. 2004.